THE GEOLOGICAL SOCIETY OF AMERICA®

First terrestrial occurrence of tistarite (Ti_2O_3): Ultra-low oxygen fugacity in the upper mantle beneath Mount Carmel, Israel

W.L. Griffin[1], S.E.M. Gain[1], D.T. Adams[1], J-X. Huang[1], M. Saunders[2], V. Toledo[3], N.J. Pearson[1], and S.Y. O'Reilly[1]
[1]ARC Centre of Excellence for Core to Crust Fluid Systems and GEMOC, Macquarie University, NSW 2109, Australia
[2]Centre for Microscopy, Characterisation and Analysis, The University of Western Australia, WA 6009, Australia
[3]Shefa Yamim (A.T.M.) Ltd., Netanya 4210602, Israel

ABSTRACT

The minimum oxygen fugacity (f_{O_2}) of Earth's upper mantle probably is controlled by metal saturation, as defined by the iron-wüstite (IW) buffer reaction (FeO → Fe + O). However, the widespread occurrence of moissanite (SiC) in kimberlites, and a suite of super-reduced minerals (SiC, alloys, native elements) in peridotites in Tibet and the Polar Urals (Russia), suggest that more reducing conditions (f_{O_2} = 6–8 log units below IW) must occur locally in the mantle. We describe pockets of melt trapped in aggregates of corundum crystals ejected from Cretaceous volcanoes in northern Israel which contain high-temperature mineral assemblages requiring extremely low f_{O_2} (IW < −10). One abundant phase is tistarite (Ti_2O_3), previously known as a single grain in the Allende carbonaceous chondrite (Mexico) and believed to have formed during the early evolution of the solar nebula. It is associated with other reduced phases usually found in meteorites. The development of super-reducing conditions in Earth's upper mantle may reflect the introduction of $CH_4 + H_2$ fluids from the deep mantle, specifically related to deep-seated volcanic plumbing systems at plate boundaries.

INTRODUCTION

The oxidation state of Earth's upper mantle is reasonably well known from estimates of the oxygen fugacity (f_{O_2}) of mineral assemblages in mantle-derived xenoliths and of magmas derived by partial melting of the mantle. These estimates range from more oxidizing than the quartz-fayalite-magnetite (QFM) buffer to near the iron-wüstite (IW) buffer; the estimated f_{O_2} generally decreases with depth relative to these buffers (Foley, 2011; Luth and Stachel, 2014). The IW buffer is widely accepted as representing the minimum f_{O_2} of the upper mantle, and several authors (Frost and McCammon, 2008, and references therein) have argued that the deeper levels of the upper mantle may be metal saturated.

However, several lines of evidence indicate that volumes with much lower f_{O_2} exist locally within the mantle. One is the common occurrence of moissanite (SiC) xenocrysts in kimberlites (Shiryaev et al., 2011; Trumbull et al., 2009), which implies f_{O_2} 6–8 orders of magnitude below the IW buffer (Ulmer et al., 1998). SiC and other phases indicative of very low f_{O_2} (nitrides, silicides, carbides) have been reported from peridotites and chromitites in ophiolites from Tibet, Myanmar, and the Polar Urals, Russia (Xu et al., 2015; Yang et al., 2015). Some have argued that the SiC in kimberlites and ultramafic rocks formed by carboreduction at high temperature (*T*) near the surface (Shiryaev and Gaillard, 2014) or by low-pressure (*P*), low-*T* reduction during serpentinization (Schmidt et al., 2014). However, moissanite inclusions in diamond (Moore and Gurney, 1989) indicate that SiC can crystallize in the deep lithospheric mantle. The occurrences in kimberlites and ophiolites are known almost entirely from mineral separates, providing little context for the phases of interest. This leaves the problems of how to produce such reducing conditions and how to preserve the reduced assemblages from oxidation by the surrounding mantle (Ulmer et al., 1998; Schmidt et al., 2014).

Here we describe super-reduced mineral assemblages, crystallized from high-*T* melts trapped in corundum aggregates (microxenoliths) ejected from Cretaceous volcanoes in northern Israel. These in situ assemblages provide insights into the processes that can produce super-reducing conditions in the upper mantle. Our analytical methods are summarized in Appendix DR2 in the GSA Data Repository[1].

SETTING AND SAMPLING

The material described here was recovered during exploration for diamond, sapphire, and other gem minerals by Shefa Yamim Ltd. (Netanya, Israel); it comes from Late Cretaceous igneous complexes on Mount Carmel in Israel and related alluvial deposits in the Kishon River catchment (southern Galilee); the volcanism has been ascribed to "hot-spot" magmas (Stein and Hofmann, 1992). Vent tuffs from one locality, the Rakefet magmatic complex (96.7 ± 0.5 Ma; Segev, 2009), have been described as similar to West African kimberlites or alkali basalt tuffisite (Yudalevich, 2007, personal commun.; Burgers, 2004; E.M.W. Skinner, 2011, personal commun.). However, wide-area scanning electron microscopy (SEM) analyses of finely crystalline lapilli (Table 1) classify them as picritic tholeiite. Heavy-mineral concentrates from the exploration campaign (Fig. DR1 in the Data Repository; Coopersmith et al., 2014) have yielded Cr-diopside, olivine, orthopyroxene, garnet, and chromite derived from garnet-spinel peridotites and pyroxenites, as well as megacrysts of Mg-ilmenite, amphibole, and diopside and less-common minerals such as diamond, moissanite (crystals to >4 mm), and corundum. All of these phases have also been found in situ in the Cretaceous tuffs. In addition to gem-quality sapphire and ruby, the erupted material includes abundant fragments of "non-gem corundum" (NGC) as much as 2.5 cm in diameter.

The NGC is typically yellow to orange-brown in color and forms aggregates of crystals with melt pockets trapped within and between them (Fig. 1A). The boundaries of the pockets are either planar or intricately lobate. Cathodoluminescence images (Fig. 1B) show that most crystals are skeletal or hopper shaped. Electron backscatter diffraction (EBSD) maps (Fig. DR2) show that the larger crystals in some fragments, or domains of smaller crystals, have subparallel *c* crystallographic axes. This growth pattern and the skeletal structures suggest the rapid growth of crystals on a substrate from an Al_2O_3-oversaturated melt, rather than the accumulation of phenocrysts from a magma. Some aggregates have been penetrated by carbon-rich fluids, producing breccias with a matrix of amorphous carbon (no Raman or EBSD signal).

The melt pockets contain >70 crystalline phases (half not described from nature). The mineral assemblages will be described in detail elsewhere; here we provide the basic data and observations that define the setting of the tistarite (Ti_2O_3) and other highly reduced phases.

[1]GSA Data Repository item 2016266, Figure DR1 (location map), Figure DR2 (EBSD images), Fig. DR3 (Raman spectra and electron-diffraction image of tistarite), Fig. DR4 (EELS spectra), and Figure DR5 (type tistarite), is available online at www.geosociety.org/pubs/ft2016.htm, or on request from editing@geosociety.org.

TABLE 1. COMPOSITIONS AND CRYSTALLOGRAPHIC DATA FROM MOUNT CARMEL, ISRAEL

	Tistarite $(Ti,Mg,Al)_2O_3$			TAZ phase $Ti_4Al_2(Zr,Si)O_{11}$			Glass in Type S melt pockets		Tuff Lapilli (EDS analyses)		Gupeiite Fe_3Si			Osbornite TiN			Unnamed boride TiB_2	
	mean n = 11	st dev	Allende Tistarite	mean n = 15	st dev	Allende Panguite	mean n = 15	st dev	mean n = 50	st dev		mean n = 40	st dev	range	mean n = 83	st dev	mean (n = 7)	st dev
SiO_2	0.05	0.05	-	1.71	0.31	1.89	43.07	1.6	43.5	1.9	Si	14.4	1.4	0–1	0.04	0.15	0.10	0.16
ZrO_2	0.62	0.39	0.44	21.1	5.74	14.61	2.06	1.0	-	-	Zr	-	-	-	-	-	-	-
Al_2O_3	1.61	0.46	1.5	18.9	1.14	7.58	22.90	2.6	13.6	2.2	Al	1.56	1.49	0–0.5	0.23	0.31	-	-
Cr_2O_3	0.05	0.04	0.06	0.05	0.03	0.54	-	-	-	-	Cr	1.62	1.84	-	-	-	0.9	1.6
Ti_2O_3	95.5	0.66	94.9	54.6	5.42	-	N/A	N/A	-	-	Ti	2.00	1.76	81–88	84.1	2.0	65.8	2.3
TiO_2	N/A	N/A	N/A	N/A	N/A	47.97	3.42	1.2	3.0	0.8	V	0.74	0.58	-	-	-	0.8	1.0
FeO	0.05	0.16	0.24	0.02	0.03	1.81	-	-	12.6	2.1	Fe	79.8	2.5	-	-	-	-	-
MnO	0.06	0.04	-	0.03	0.02	-	0.13	0.1	-	-	Mn	0.35	0.41	-	-	-	-	-
MgO	1.92	0.39	2.06	1.79	0.45	5.54	4.84	1.4	-	-	N	-	-	10.5–17	15.5	1.9	-	-
CaO	0.12	0.10	0.10	0.38	0.17	3.34	15.29	1.4	15.0	2.9	B	-	-	-	-	-	31.7	2.7
Na_2O	0.00	0.01	-	0.00	0.00	-	0.41	0.3	10.3	2.3								
K_2O	0.01	0.01	-	0.01	0.01	-	0.93	0.3	0.2	0.2								
Sc_2O_3	0.11	0.05	-	0.58	0.14	10.67	-	-	0.5	0.5								
La_2O_3	0.01	0.01	-	0.01	0.02	-	0.78	0.1	-	-								
Ce_2O_3	0.04	0.03	-	0.03	0.03	-	1.58	0.3	-	-								
Nd_2O_3	0.01	0.01	-	0.02	0.03	-	0.46	0.12	-	-								
HfO_2	0.03	0.04	-	0.44	0.14	0.28	-	-	-	-								
UO_2	0.03	0.02	-	0.15	0.08	-	0.12	0.05	-	-								
ThO_2	0.01	0.01	-	0.07	0.03	-	0.60	0.1	-	-								
Y_2O_3	0.00	0.01	-	0.40	0.12	5.38	0.38	0.20	-	-								
SO_2	0.00	0.01	-	0.01	0.01	-	1.24	0.4	1.2	0.4								
Total	100.23		99.30	99.89		99.43	96.59		98.70			100.47			99.87		99.30	
Crystal system	Trigonal			Orthorhombic (assumed)								Cubic		Cubic			Hexagonal	
Space Group	R3c			Pbca (Assumed)								Fm3m		Fm3m			P6/mmm	
Ti (EELS)	3+			3+								3+		3+			2+	

Note: St. Dev., one standard deviation on the mean. Missing values, below detection limits, or not reported in primary references. N/A, not applicable. EDS and EELS are defined in the text. Ti(EELS) is the measured valence state of Ti in the given phase.

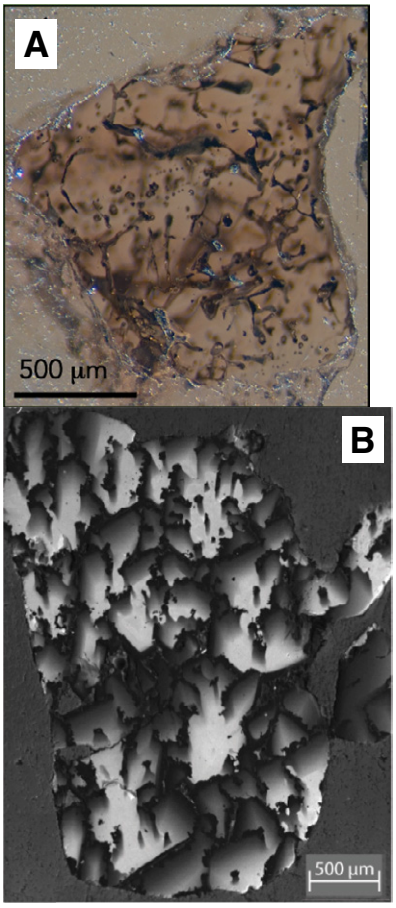

Figure 1. Non-gem corundum from Mount Carmel, Israel. A: Crystal aggregate with three-dimensional network of melt inclusions (dark blebs, curvilinear strings). B: Cathodoluminescence image of aggregate of zoned crystals; darker areas are higher in Ti and typically adjoin melt pockets.

The pockets are of three general types. Type S, the most abundant, has crystalline phases, commonly including tistarite, set in a Ca-K-Al-Si–oxide matrix (Table 1; Fig. 2), apparently glass; it gives no Raman signal. Some pockets show quench structures with radiating blades or needles of anorthite and rare earth element–rich phases in the glass. In others, the matrix has crystallized to an assemblage including zirconolite, fassaite, anorthite, and undescribed phases. None of the silicate or oxide phases in the type S melt pockets contains detectable Fe or Ni.

Type A melts (Fig. 3) are Fe-Ti-Si-C-P alloys which have crystallized to phases including gupeiite (Fe_3Si), FeTi(Si,P), FeTiSi, FeTi, and TiC (khamrabaevite). Native vanadium occurs together with hibonite ($CaAl_{12}O_{19}$).

Type N (Fig. 4) is represented by osbornite (TiN, 12.5%–16% N; Table 1). The unnamed boride TiB_2 is intergrown with TiN; the identity of both phases is confirmed by electron diffraction (Table 1). Type N assemblages may occur alone in complex three-dimensional (3-D) networks or intergrown with type S (Fig. 4).

The textural relationships in and among the melt pockets suggest that these "melts" were mutually immiscible. They can be found in different areas of single necked-down inclusions and in separate inclusions in the same corundum grain; the apparent separation may simply reflect 2-D sectioning of 3-D structures (Fig. 1A). The quench structures imply that crystallization was halted by the eruption of the host magma.

OCCURRENCE OF TISTARITE

Tistarite is one of the most common phases in the type S pockets (Figs. 2 and 4). Its composition (Table 1) is similar to that of the type grain (Ma and Rossman, 2009; Fig. DR5), even in terms of the minor elements Mg, Al, and Zr, but it contains essentially no Fe. Its Raman spectrum is identical to those of the type material and synthetic Ti_2O_3 (Fig. DR3). Transmission electron microscopy (TEM) electron diffraction data are consistent with the reported space group R-3c (Table 1; Ma and Rossman, 2009). Its electron energy loss (EELS) spectrum (Fig. DR4) confirms that Ti is present as Ti^{3+}. Most grains are rounded (Figs. 2 and 4), but some have straight edges and/or blocky outlines, suggesting that they originally formed as euhedral crystals but were partially resorbed.

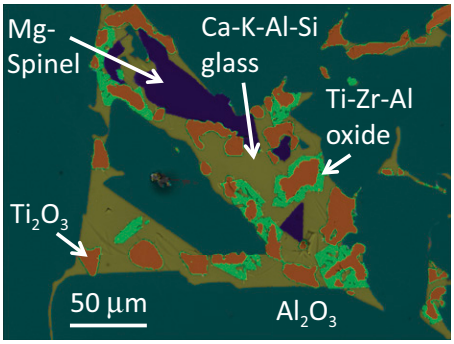

Figure 2. Energy-dispersive X-ray spectroscopy–scanning electron microscopy composite element map of type S melt pocket in corundum matrix from Mount Carmel, Israel, showing tistarite (Ti_2O_3), some rimmed by Ti-Zr-Al oxide, and crystal of Mg-spinel in matrix of Ca-Al-Si glass (Table 1). Note combination of straight and lobate boundaries to melt pocket, defined by crystal faces of adjacent corundum (Al_2O_3) crystals.

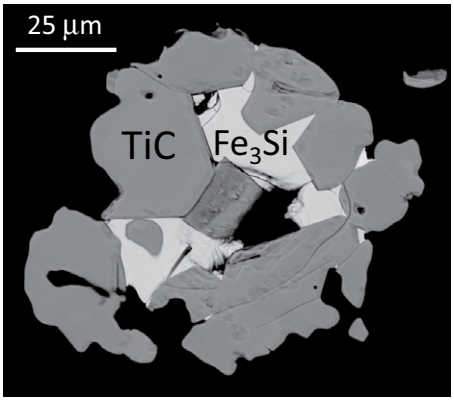

Figure 3. Backscattered electron (BSE) image of type A melt inclusion in corundum from Mount Carmel, Israel; crystals of TiC surround a pool of Fe_3Si.

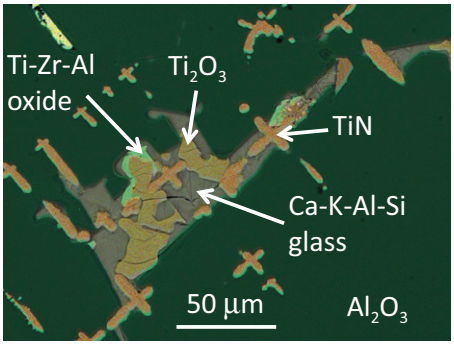

Figure 4. Energy-dispersive X-ray spectroscopy–scanning electron microscopy composite element map of type N and type S melts from Mount Carmel, Israel. TiN appears to reside in cavities in skeletal crystal; type S pocket shows both straight and locally lobate boundaries, characteristic of skeletal growth. Dark needles in glass are anorthite.

Tistarite grains commonly are rimmed by a Ti-Al-Zr oxide with scalenohedral crystal outlines (informal name TAZ; Fig. 2; Table 1) and the general composition $Ti_4Al_2ZrO_{11}$. Its stoichiometry and EELS spectrum (Fig. DR4) indicate that Ti is present as Ti^{3+}. Inter-element correlations suggest that Mg, Ca, and Al substitute for Ti, and Si for Zr. TAZ may be an analogue of panguite [$(Ti^{4+},Sc,Al,Mg,Zr,Ca)_{1.8}O_3$; Ma et al., 2012], but TAZ contains little Sc, and Ti^{3+} instead of Ti^{4+}. TEM electron diffraction data suggest that while TAZ is related to panguite, its space group and unit cell are not a direct match. TAZ will be submitted to the International Mineralogical Association for approval as a new mineral.

DISCUSSION

Tistarite was originally described from a single 12 × 5 µm grain in the Allende CV3 carbonaceous chondrite (Mexico), associated with TiC and corundum (Ma and Rossman, 2009; Fig. DR5). As noted above, TiC also is abundant in the melt pockets described here. Other phases found in both primitive meteorites and the Mount Carmel NGC include wassonite (TiS), a Ti analogue of barringerite [$(Fe,Ti)_2P$], grossite ($CaAl_4O_7$), and hibonite ($CaAl_{12}O_{19}$). Corundum, hibonite, TiC, and tistarite in carbonaceous chondrites condensed early in the evolution of the solar nebula (Grossman et al., 2008). The key link between the meteoritic and terrestrial occurrences is their very low f_{O_2}; in the early solar nebula, this was produced by the streaming of hydrogen in the solar wind (Grossman et al., 2008). We suggest by analogy that in the Mount Carmel setting, H_2 (and/or CH_4) was supplied from the deeper levels of the upper mantle as part of the volcanic plumbing system (see below). We do not suggest an extraterrestrial origin for the Mount Carmel material; the volcanic association is obvious.

Temperatures can be estimated for some of the Mount Carmel assemblages based on experiments at 1 atm. Ti_2O_3 crystallizes in the Ti-O system between ~1800 and 1600 °C (Das et al., 2002). Fe_3Si can crystallize in the binary system between ~1400 and 1200 °C, and FeTiSi occurs on the ternary liquidus from ~1530 to 1150 °C (Weitzer et al., 2008). The late crystallization of anorthite in type S melt pockets implies cooling of the system through the peritectic reaction corundum + melt → anorthite; this indicates temperatures of 1450–1550 °C and pressures between ~9 and 29 kbar (30–100 km depth; Goldsmith, 1980). The heavy mineral–xenolith suite in the tuffs shows that the magmas sampled a thin (<100 km), hot lithospheric mantle (Apter, 2014; our unpublished data). These constraints indicate that the NGC aggregates crystallized at magmatic *T* within the lithospheric mantle; the low f_{O_2} does not reflect shallow carboreduction (Shiryaev and Gaillard, 2014) nor low-*T* serpentinization (Schmidt et al., 2014).

The SiC grains found in debris from the Rakefet magmatic complex are much larger (up to 4.1 mm) than the melt pockets but similar in size to the NGC grains. Moissanite has been found included in corundum and in the carbon-rich breccia veins; we suggest that the SiC and the NGC comprised related parts of a single magmatic system.

The crystallization of the NGC and the SiC may reflect mixing between mantle-derived CH_4 and mafic magmas in a volcanic plumbing system. Reactions of the type SiO_2 (in silicate melt) + CH_4 → SiC + $2H_2O$ would desilicate the magma and drive f_{O_2} below IW, leading to precipitation of Fe, supersaturation in Al_2O_3, and the rapid crystallization of corundum. Reactions such as $2CH_4 + H_2O \rightarrow C + CO_2 + 4H_2$ would deposit carbon and further lower f_{O_2} through the liberation of hydrogen, analogous to the industrial process used to produce H_2. At mantle depths, H_2 is immiscible in H_2O (Bali et al., 2013), allowing rapid migration into the porous corundum aggregates. The buildup of CO_2 produced by such reactions may have contributed to the explosive end to the crystallization process.

The apparent resorption of tistarite crystals and the presence of even more reduced phases suggest a progressive drop in f_{O_2} during crystallization. Ti_2O_3 becomes stable at roughly the same f_{O_2} as SiC (IW ~–7), but the occurrence of native vanadium in some melt pockets implies f_{O_2} of at least IW –8, strongly suggesting the presence of hydrogen (Ulmer et al., 1998). The occurrence of TiO in some type N pockets indicates even lower f_{O_2} (≤IW –13; Ulmer et al., 1998). The decrease in f_{O_2} could reflect the streaming of H_2 through the porous corundum aggregates as the pockets of trapped melt were evolving and shrinking in volume due to the crystallization of corundum.

This system could have been effectively isolated from the surrounding peridotitic mantle by crystallization of the NGC, e.g., along the walls of magma conduits or on the floors of magma chambers, preserving SiC and other highly reduced phases from oxidation by the surrounding mantle until the eruption of the host magmas.

The super-reduced assemblages described here are broadly similar to those in the chromitites and peridotites of Tibetan and Polar Urals ophiolites (Yang et al., 2015), which may have been subducted into the mantle transition zone and exhumed during slab rollback (Griffin et al., 2016). Although tistarite has not been reported from these localities, some of the exotic Ti-bearing phases in the Tibetan chromitites have been found only in grains of corundum (Xu et al., 2015).

In another example, mafic pumice from the A.D. 2013–2014 Tolbachik fissure eruption on the Kamchatka Peninsula (Russia) contains abundant microdiamonds (Karpov et al., 2014), similar to those from the Tibetan ophiolites

(Howell et al., 2015). The diamonds are accompanied by moissanite and Ti-bearing corundum. Ishimaru et al. (2009) described metal-saturated peridote xenoliths from the Avacha volcano on Kamchatka and ascribed them to reduction by H_2-rich fluids from below the mantle wedge. Gorshkov et al. (1995) reported diamond (carbonado) in ejecta from Avacha.

The presence of similarly reducing conditions, associated with Ti-corundum, suggests the operation of a common process in these widely separated areas. All of these areas feature mafic volcanism related to plate boundaries (deep subduction zones and translithospheric faults; e.g., the Dead Sea transform). Mantle upwellings accompanying the rise of magmas, especially in areas stirred by subducting slabs, may be expected to release C-O-H fluids; if the mantle is metal saturated, such fluids will be dominated by $CH_4 \pm H_2$ (Frost and McCammon, 2008). Interaction between deep-seated magmas and $CH_4 \pm H_2$ fluids in volcanic plumbing systems, to produce local ultra-reducing conditions, therefore may be a common phenomenon.

The samples described here represent a mantle environment and a part of the global carbon cycle that were previously unrecognized. Further studies of the trace minerals in explosive volcanic eruptions are required to evaluate how widespread such processes may be.

ACKNOWLEDGMENTS

We are grateful to John Ward and Dave Apter for advice on the geology and petrology of material kindly provided by Shefa Yamim Ltd. (Israel), to Takako Satsukawa for tutoring in EBSD, to D. Jacob and S. Foley for discussions about oxygen fugacity, to Steve Craven and Manal Bebbington for sample preparation, and to Simon Redfern and editor J. Brendan Murphy for useful comments. This study used instrumentation funded by Australian Department of Education, Science and Training (DEST) Systemic Infrastructure Grants, Australian Research Council Linkage Infrastructure, Equipment and Facilities (ARC LIEF), Australia National Collaborative Research Infrastructure Strategy (NCRIS/AuScope), Macquarie University, and industry partners. We acknowledge the scientific and technical assistance of the Australian Microscopy and Microanalysis Research Facility at the Centre for Microscopy, Characterization and Analysis, a facility funded by The University of Western Australia, and State and Commonwealth Governments. This is contribution 830 from the ARC Centre of Excellence for Core to Crust Fluid Systems (http://ccfs.mq.edu.au) and 1039 from the GEMOC ARC National Key Centre (http://gemoc.mq.edu.au).

REFERENCES CITED

Apter, D., 2014, High pressure indicator minerals from the Rakefet Magmatic Complex (RMC), Mt. Carmel, Israel, *in* Proceedings of the Geological Society of South Africa Kimberley Diamond Symposium, Extended Abstract.

Bali, E., Audetat, A., and Keppler, H., 2013, Water and hydrogen are immiscible in Earth's mantle: Nature, v. 495, p. 220–222, doi:10.1038/nature11908.

Burgers, K.M., 2004, The petrography and geochemistry of 4 samples from the Mount Carmel-01 kimberlite, Shefa Yamim, Israel: DeBeers Group Internal Report 513/003/0001, 12 p.

Coopersmith, H., Toledo, V., Fritsch, E., Ward, J., De Wit, M., and Spaggiari, R., 2014, Geology and exploration of gem deposits at Mt Carmel, Northern Israel: Natural moissanite, sapphire, ruby and diamond: Geological Society of America Abstracts with Programs, v. 46, no. 6, p. 416, Abstract 165-3.

Das, K., Choudhury, P., and Das, S., 2002, The Al-O-Ti (aluminum-oxygen-titanium) system: Journal of Phase Equilibria, v. 23, p. 525–536, doi:10.1361/105497102770331271.

Foley, S.F., 2011, A reappraisal of redox melting in the Earth's mantle as a function of tectonic setting and time: Journal of Petrology, v. 52, p. 1363–1391, doi:10.1093/petrology/egq061.

Frost, D.J., and McCammon, C.A., 2008, The redox state of Earth's mantle: Annual Review of Earth and Planetary Sciences, v. 36, p. 389–420, doi:10.1146/annurev.earth.36.031207.124322.

Goldsmith, J.R., 1980, The melting and breakdown reactions of anorthite at high pressures and temperatures: The American Mineralogist, v. 65, p. 272–284.

Gorshkov, A., Seliverstov, V.A., Baikov, A.I., Anikin, L.P., Sivtsov, A.V., and Duninbarkvskii, R.L., 1995, Crystallochemistry and genesis of carbonado from the melanocratic basaltoids of the Avacha volcano, Kamchatka Peninsula: Geology of Ore Deposits, v. 37, p. 44–55.

Griffin, W.L., et al., 2016, Mantle recycling: Transition zone metamorphism of Tibetan ophiolitic peridotites and its tectonic implications: Journal of Petrology, v. 57, p. 655–684, doi:10.1093/petrology/egw011.

Grossman, L., Beckett, J.R., Fedkin, A.V., Simon, S.B., and Ciesla, F.J., 2008, Redox conditions in the solar nebula: Observational, experimental, and theoretical constraints: Reviews in Mineralogy and Geochemistry, v. 68, p. 93–140, doi:10.2138/rmg.2008.68.7.

Howell, D., Griffin, W.L., Gain, S., Stern, R.A., Huang, J.-X., Yang, J., Pearson, N.J., and O'Reilly, S.Y., 2015, Diamonds in ophiolites: Contamination or a new diamond growth environment?: Earth and Planetary Science Letters, v. 430, p. 284–295, doi:10.1016/j.epsl.2015.08.023.

Ishimaru, S., Arai, S., and Shukuno, H., 2009, Metal-saturated peridotite in the mantle wedge inferred from metal-bearing peridotite xenoliths from Avacha volcano, Kamchatka: Earth and Planetary Science Letters, v. 284, p. 352–360, doi:10.1016/j.epsl.2009.04.042.

Karpov, G.A., Silaev, V.I., Anikin, L.P., Rakin, V.I., Vasil'ev, E.A., Filatov, S.K., Petrovskii, V.A., and Flerov, G.B., 2014, Diamonds and accessory minerals in products of the 2012–2013 Tolbachik fissure eruption: Journal of Volcanology and Seismology, v. 8, p. 323–339, doi:10.1134/S0742046314060049.

Luth, R., and Stachel, T., 2014, The buffering capacity of lithospheric mantle: Implications for diamond formation: Contributions to Mineralogy and Petrology, v. 168, 1083, doi:10.1007/s00410-014-1083-6.

Ma, C., and Rossman, G.R., 2009, Tistarite, Ti_2O_3, a new refractory mineral from the Allende meteorite: The American Mineralogist, v. 94, p. 841–844, doi:10.2138/am.2009.3203.

Ma, C., Tschauner, O., Beckett, J.R., Rossman, G.R., and Liu, W., 2012, Panguite, $(Ti^{4+},Sc,Al,Mg,Zr,Ca)_{1.8}O_3$, a new ultra-refractory titania mineral from the Allende meteorite: Synchrotron micro-diffraction and EBSD: The American Mineralogist, v. 97, p. 1219–1225, doi:10.2138/am.2012.4027.

Moore, R.O., and Gurney, J.J., 1989, Mineral inclusions in diamond from the Monastery kimberlite, South Africa, *in* Ross, J., ed., Kimberlites and Related Rocks, Volume 2: Their Mantle/Crust Setting, Diamonds and Diamond Exploration: Cambridge, UK, Blackwell Scientific, Geological Society of Australia Special Publication 14, p. 1029–1041.

Schmidt, M.W., Gao, C., Golubkova, A., Rohrbach, A., and Connolly, J.A.D., 2014, Natural moissanite (SiC)—A low temperature mineral formed from highly fractionated ultra-reducing COH-fluids: Progress in Earth and Planetary Science, v. 1, 27, doi:10.1186/s40645-014-0027-0.

Segev, A., 2009, $^{40}Ar/^{39}Ar$ and K-Ar geochronology of Berriasian–Hauterivian and Cenomanian tectonomagmatic events in northern Israel: Implications for regional stratigraphy: Cretaceous Research, v. 30, p. 810–828, doi:10.1016/j.cretres.2009.01.003.

Shiryaev, A.A., and Gaillard, F., 2014, Local redox buffering by carbon at low pressures and the formation of moissanite–natural SiC: European Journal of Mineralogy, v. 26, p. 53–59, doi:10.1127/0935-1221/2013/0025-2339.

Shiryaev, A.A., Griffin, W.L., and Stoyanov, E., 2011, Moissanite (SiC) from kimberlites: Polytypes, trace elements, inclusions and speculations on origin: Lithos, v. 122, p. 152–164, doi:10.1016/j.lithos.2010.12.011.

Stein, M., and Hofmann, A.W., 1992, Fossil plume head beneath the Arabian lithosphere?: Earth and Planetary Science Letters, v. 114, p. 193–209, doi:10.1016/0012-821X(92)90161-N.

Trumbull, R.B., Yang, J.-S., Robinson, P.T., Di Pierro, S., Vennemann, T., and Wiedenbeck, M., 2009, The carbon isotope composition of natural SiC (moissanite) from the Earth's mantle: New discoveries from ophiolites: Lithos, v. 113, p. 612–620, doi:10.1016/j.lithos.2009.06.033.

Ulmer, G.C., Grandstaff, D.E., Woerman, E., Gobbels, M., Schonitz, M., and Woodland, A.B., 1998, The redox stability of moissanite (SiC) compared with metal-metal oxide buffers at 1773K and at pressures up to 90 kbar: Neues Jahrbuch für Mineralogie: Abhandlung, v. 172, p. 279–307.

Weitzer, F., Schuster, J.C., Naka, M., Stein, F., and Palm, M., 2008, On the reaction scheme and liquidus surface in the ternary system Fe–Si–Ti: Intermetallics, v. 16, p. 273–282, doi:10.1016/j.intermet.2007.10.006.

Xu, X., Yang, J., Robinson, P.T., Xiong, F., Ba, D., and Guo, G., 2015, Origin of ultrahigh pressure and highly reduced minerals in podiform chromitites and associated mantle peridotites of the Luobusa ophiolite, Tibet: Gondwana Research, v. 27, p. 686–700, doi:10.1016/j.gr.2014.05.010.

Yang, J.S., Meng, F., Xu, S., Robinson, P.T., Dilek, Y., Makeyev, A.B., Wirth, R., Wiedenbeck, M., and Cliff, J., 2015, Diamonds, native elements and metal alloys from chromitites of the Ray-Iz ophiolite of the Polar Urals: Gondwana Research, v. 27, p. 459–485, doi:10.1016/j.gr.2014.07.004.

Manuscript received 21 March 2016
Revised manuscript received 19 July 2016
Manuscript accepted 23 July 2016

Printed in USA